Potential of Interdigitated Back-Contact Silicon Heterojunction Solar Cells for Liquid Phase Crystallized Silicon on Glass with Efficiency above 14%

Cham Thi Trinh[a,*], Natalie Preissler[a,b], Paul Sonntag[a], Martin Muske[a], Klaus Jäger[c], Martina Trahms[a], Rutger Schlatmann[b], Bernd Rech[a], Daniel Amkreutz[a]

[a] Institute for Silicon Photovoltaics / Helmholtz-Zentrum Berlin für Materialien und Energie GmbH, Berlin, Germany

[b] PVcomB / Helmholtz-Zentrum Berlin für Materialien und Energie GmbH, Berlin, Germany

[c] Young Investigator Group Nano-SIPPE / Helmholtz-Zentrum Berlin für Materialien und Energie GmbH, Berlin, Germany

[*]Corresponding author. Tel: +49 (0)30 8062-41385, *Email address*: cham.trinh@helmholtz-berlin.de

Abstract

Liquid phase crystallization of silicon (LPC-Si) on glass is a promising method to produce high quality multi-crystalline Si films with macroscopic grains. In this study, we report on recent improvements of our interdigitated back-contact silicon heterojunction contact system (IBC-SHJ), which enabled open circuit voltages as high as 661 mV and efficiencies up to 14.2% using a 13 µm thin n-type LPC-Si absorbers on glass. The influence of the BSF width on the cell performance is investigated both experimentally and numerically. We combine 1D optical simulations using GenPro4 and 2D electrical simulations using Sentaurus™ TCAD to determine the optical and electrical loss mechanisms in order to estimate the potential of our current LPC-Si absorbers. The simulations reveal an effective minority carrier diffusion length of 26 µm and further demonstrate that a doping concentration of 4×10^{16} cm^{-3} and a back surface field width of 60 µm are optimum values to further increase cell efficiencies.

1. Introduction

Renewable energy revolution has boosted the growth of photovoltaic industry in recent years. According to international technology roadmap for photovoltaics (ITRPV), the levelized cost of electricity (LCOE) will continuously decrease and the price of large-scale systems is estimated to drop to 680 US$/KWp in the next 10 years [1]. One main key for cost reduction is saving material during the cell fabrication process, in particular, Silicon as it accounts for up to 40% of the cell price [2]. Therefore, in the past a lot of technologies were developed to fabricate high-quality c-Si thin films [3], such as solid phase crystallization (SPC) [4], seed layer approach (i.e. metal induced crystallization (ALILE) [5]) or direct crystalline epitaxial growth [6]. However, these technologies suffered from a high defect density in the bulk, limiting the achievable open circuit voltage (V_{oc}) to 560 mV [7]. Liquid phase crystallization of silicon

(LPC-Si) is a promising method to grow large-grain silicon film on glass by using line-shaped energy sources, such as a laser or an electron beam [8]. This method is able to crystallize thin Si films with thicknesses as high as 40 µm and with grain size up to centimeters in length and a few millimeters in width [9-11]. A high open circuit voltage (V_{oc}) of 656 mV was achieved with a 10 µm-thick LPC-Si absorber [10], which is close to the V_{oc} of conventional multi-crystalline Si [10, 12]. This absorber was crystallized by an electron beam and a stable efficiency of 11.5% was obtained for a back-contacted solar cell design [10]. The LPC-Si technique based on a continuous wave electron beam was developed by Amkreutz *et al.*. A later study showed no detectable difference in bulk quality of the Si absorber crystallized by laser or e-beam [13]. Optimization of the crystallization process and a mature interface engineering of the intermediate layers (ILs) between glass and Si are crucial steps to enhance absorber quality. ILs have to fulfill a variety of requirements, such as providing adhesion during the crystallization process, preventing impurity diffusion from glass, acting as antireflective coating, and passivating interface defects. The ILs are mainly based on amorphous silicon oxide (SiO_x), amorphous silicon nitride (SiN_x), amorphous silicon oxynitride (SiO_xN_y), amorphous silicon carbide (SiC_x) and aluminum oxide (AlO_x) prepared by plasma-enhanced chemical vapor deposition (PECVD), reactive RF-magnetron sputtering (PVD) or atomic layer deposition (ALD) [7, 14-20]. Dore *et al.* found that the layer in direct contact to the Silicon plays a significant role on enhancing electronic quality of the absorber and the best efficiency for LPC-Si solar cell on glass was realized by a triple stack of $SiO_x/SiN_x/SiO_x$ (ONO) [16]. Amkreutz *et al.* also reported a V_{oc} above 620 mV and an efficiency up to 11.8% for a back-contacted solar cell with laser crystallized Si on glass with a sputtered ONO stack [13]. For PECVD ONO layers, an annealing step needs to be conducted in order to release mobile hydrogen in ILs, which is detrimental for crystallization. An efficiency of 12.1% was obtained with a LPC-Si absorber using PECVD $SiN_x/SiO_x/SiO_xN_y$ for a point contact cell assisted by a light trapping scheme [20]. Recently, Preissler *et al.* realized that a nitrogen–rich SiN_x layer in a PECVD ONO stack layer enables adhesion without prior annealing [15]. The absence of Si-H bonds in the SiN_x structure enhances its stability during crystallization by avoiding H desorption, thus, preventing peeling off. The interdigitated back-contact silicon heterojunction (IBC-SHJ) solar cell based on LPC-Si on glass was firstly introduced by Sonntag *et al.* [21]. However, the obtained efficiencies < 10% were limited by low fill factors (< 55%). Recently, based on ONO IL developed by Preissler *et al.*, a high efficiency of 13.2% was achieved for IBC-SHJ solar cells for 13 µm-thick n-type LPC-Si on glass [22, 23]. This outstanding result was obtained for both high and low doping Si absorber with fill factors of 74.7% and 67.2%, respectively, thanks to improvement in IL engineering, optimum geometric design and cell fabrication processes. However, optimization of the contact system geometries has not been clarified yet. For IBC-SHJ cells, all contacts are placed at the back-side of the absorber, therefore, an ideal geometry is necessary to collect as much current as possible without causing resistive loss or electric shading. For the best cell efficiency with an emitter ratio of 90% (back surface field (BSF) width of 120 µm), almost no current was collected under the BSF finger region due to limitations of the minority diffusion length (< 30 µm). Analysis on light beam induced current (LBIC) mapping revealed that 11% of the loss in short circuit current density (J_{sc}) is dedicated to the BSF fingers and their surrounding area. Therefore, in this study, we focus on developing the geometric structure for IBC-SHJ solar cells for LPC-Si on glass. We firstly work on numerical simulation for the IBC structure to examine the effect of BSF width

on the cell performance. Then, experimental results of real IBC-SHJ cells with various BSF widths are reported.

2. Sample preparation and characterization

2.1. Absorber fabrication

Firstly, 10×10 cm^2 cleaned aluminosilicate glass substrates (Corning Eagle XG, 1.1 mm thickness) were coated with different ILs. The ILs used in this study include SiO_x/SiN_x (ON), $SiO_x/SiN_x/SiO_x$ (ONO) with a 15 nm-thick SiO_x passivation layer and ON(ON) stack layer in which SiO_x/SiN_x was oxidized by a N_2O plasma for 10 min. Due to this oxidation process a 10 nm-thick SiO_xN_y film can be deposited in a controlled and reproducible way. This process is also considered to increase the homogeneity of the layer in direct contact to the absorber and thus, to provide less scattering of the cell results. Details on the interlayer development and deposition process are described in Ref. [24]. A 14.7 µm-thick undoped silicon layer was deposited on top of the ILs using electron-beam evaporation at a heater temperature of 600°C and deposition rate of roughly 600 nm/s. An 80 nm-thick phosphorous doped a-Si:H (n+) film was then deposited acting as doping source for the LPC-Si absorber layer. Samples were finally coated with a 100 nm SiO_x layer to avoid dewetting during crystallization under vacuum conditions. All layers were deposited using a Von Ardenne CS400PS integrated CVD/PVD cluster tool. The crystallization process was carried out in a vacuum system using a line-shape continuous wave diode laser (808 nm) at a scan speed of 3 mm/s (power density <3 kW/cm^2). Vacuum conditions were chosen to avoid contamination during the crystallization process. In accordance with the geometry of the laser line of 52×0.3 mm^2, samples were cut into four 5×5 cm^2 subsamples. Before crystallization, samples were preheated to 500°C surface temperature to reduce thermal stress during crystallization. After crystallization, stress in the glass substrates was released by rapid thermal annealing at 950°C. The SiO_x cap was removed with diluted hydrofluoric acid (HF, 5%) before a hydrogen plasma treatment was performed to passivate the Si bulk. Damaged Si was removed with an aqueous solution consisting of HF, nitric acid (HNO_3), and phosphoric acid (H_3PO_4). Subsequently the samples were textured with a potassium hydroxide (KOH)-based solution with Alkatex free+ additive at 80°C for 3 min, resulting in pyramid sizes of 1.5-2.0 µm on initial (100) surface. For other surface orientations, the pyramids are tilted by various angles up to flat surfaces for the (111) orientation. The final thickness of the Si absorber is around 13 µm.

2.2. IBC-SHJ cell fabrication

For this study, cells were designed with various BSF widths (W_{BSF}) of 240 µm, 120 µm, 90 µm and 60 µm. The emitter finger width ($W_{emitter}$) was kept unchanged at 1080 µm. All cells were designed to have an area of (1×0.6) cm^2. The cell fabrication consists of several photolithography steps (Resist: Microchemicals AZ 4533, mask aligner: MA6 SÜSS MicroTec) used for structuring. Top views of the back side of a cell after each layer structuring step are shown in Fig. 1 (a)-(c). The schematic cross section of the cell is depicted in Fig. 1 (d). We followed the cell fabrication processes as described in Refs. [20, 22]. The samples were cleaned with a standard RCA cleaning process before cell fabrication. Subsequently, a-Si:H (i/p^+) emitter layers were deposited by PECVD. The layers were then structured by photolithography.

A metal-ion-free tetramethylammonium hydroxide (TMAH) 2.5% solution was employed for development. The hetero-emitter was etched using an aqueous solution consisting of HF, HNO_3, and H_3PO_4. After another RCA cleaning step, the samples were covered with an a-Si:H (n^+) layer by PECVD and then structured to form the BSF. We used TMAH 2.5% solution for developing and etching the exposed BSF areas [22]. The overlap of the a-Si:H (p^+) and a-Si:H (n^+) regions is 15 µm in the mask design and it reduces to 8 µm due to over-etching after patterning. Please notice that W_{BSF} doesn't include this overlap width, as shown in Fig. 1(d). These intrinsic, boron doped (for emitter) and phosphorus doped (for BSF) Si-films have thicknesses of 7 nm, 15 nm and 10 nm on the textured surface, respectively. Electrodes of 120-nm thick indium-tin-oxide (ITO) and 1 µm-thick silver (Ag) films were deposited in a sputtering process. A final photolithography step was done to structure the electrodes on the emitter and BSF. We employed Hydrochloric acid (HCl) (20%) for ITO etching and diluted mixture of ammonia solution (NH_4OH) and hydrogen peroxide (H_2O_2) for Ag etching. In order to cure damage during ITO sputtering, samples were annealed in an oven at 180 ^oC for 20 min.

2.3. Cell characterization

Current-voltage (*J-V*) curves were obtained using an AAA-rated solar simulator of type Wacom WXS-156S-L2, AM1.5GMM with dual sources (halogen and xenon lamp). *Suns-Voc* measurements were performed by Sinton Instruments (Boulder, CO, USA). Reflection (*R*) and transmission (*T*) spectra were measured with a PerkinElmer LAMBDA 1050 spectrophotometer. The doping concentration (N_D) of the samples was calculated via the sheet resistance, which was obtained by a four point probe measurement. The sheet resistance was measured in at least 12 different points for each 5×5 cm^2 sample and the average value was taken from all samples. Hole and electron mobilities are assumed to be at 80% of the hole and electron mobilities of mono c-Si, which is in good agreement with measured mobilities obtained by Hall measurements [22]. The series resistance (R_s) was determined by comparing dark and illuminated *J-V* curves [25]. The surface morphology of the textured absorbers was obtained by an atomic force microscope. The a-Si:H film thickness and the optical properties (refractive index and extinction coefficient) were obtained by spectroscopic ellipsometry, using Tauc-Lorentz model.

3. Results and discussion

3.1. 2D simulation

The effect of W_{BSF} on the performance of IBC-SHJ cells was simulated with the TCAD-Sentaurus^{TM} device simulator [26]. Since our samples are back-side textured, it is challenging to simulate the correct optical properties. Therefore, a photon generation profile would be more appropriate to display photon absorption in a real IBC cell. One problem is that the absorption extracted from measured reflectance and transmission data includes parasitic absorption of the supporting layers, such as a-Si:H or ITO. In order to determine the absorption in these layers, we performed optical simulations with the MATLAB-based program GenPro4, which is developed at the Delft University of Technology [27], and utilizes the transfer-matrix method. The pyramidal morphology of the samples was taken into account using the ray tracing model included in GenPro4. We used complex refractive index (*n*, *k*) data of glass [28], c-Si [29], ITO

[30], and Ag [31] reported in literature. The optical properties of all other layers were individually determined by spectroscopic ellipsometry. The absorption spectrum of each layer is shown in Fig. 2 (b). The blue dotted curve displays experimentally measured absorption (*1-R-T*) of a real IBC cell. One can see a good match between simulated and experimental data.

Due to multiple reflections in the layer stack, the generation profile in the silicon layer cannot be derived with the Lambert-Beer law. We estimated the generation profile in the silicon layer with the following assumption: light passes through the layer with an exponentially decaying intensity. At the back, the light is reflected back into the layer and again, the intensity decays exponentially and so forth, which mathematically is expressed via a geometric series. Following this assumption we can calculate the generation profile $G(z,\lambda)$,

$$G(z,\lambda) = \Phi_{\mathrm{ph},\lambda} A(\lambda)\alpha \frac{\exp(-\alpha z)+\exp(-2dz)\exp(\alpha z)}{1-\exp(-2dz)}, \quad (1)$$

where $\Phi_{\mathrm{ph},\lambda}$ is the spectral photon flux from the AM 1.5 solar spectrum, $A(\lambda)$ is the absorption in the silicon layer extracted from GenPro4, $\alpha = \alpha(\lambda)$ is the absorption coefficient of silicon and d is the thickness of the silicon layer. The reflectivity of both sides of the Si layer were estimated to be 100%.

TCAD-Sentaurus™ was used to simulate the IBC cell performance. A front surface recombination velocity (SRV_{front}) of 200 cm/s is assumed since it was found to be a reasonable value for the present passivation quality of ONO ILs [22, 23]. For LPC-Si electrical quality, we used the Scharfetter model, in which Shockley-Read Hall (SRH) lifetime is doping dependent [26, 32, 33]. The Shockley-Read-Hall (SRH) lifetime is calculated as:

$$\tau = \tau_{\min} + \frac{\tau_{\max} - \tau_{\min}}{1+\left(\frac{N_D+N_A}{N_{ref}}\right)^{\gamma}}. \quad (2)$$

τ_{min} = 0 and γ = 1 were used for c-Si [32, 33]. N_{ref} of 7×10^{15} cm^{-3} and τ_{max} of 395 µs was found by fitting equation (2) with experimental carrier lifetime of c-Si [32], which has a bulk lifetime higher than LPC-Si. Therefore, suitable N_{ref} and τ_{max} values for LPC-Si need to be determined. To meet the purpose, we varied τ_{max} and N_{ref} values to simulate J_{sc} and V_{oc} of the 13.2% IBC cells with low doped and high doped absorber from Ref. [22]. The interface of a-Si:H/ LPC-Si was described by introducing a thin defect layer. This defect layer is necessary to result in a good match between experimental and simulated V_{oc} [13]. A τ_{max} of 2.1 µs and N_{ref} of 7.5×10^{16} cm^{-3} resulted in the best fit for these samples, as shown in Table 1. As a result, τ of 1.8 µs and 0.8 µs are obtained for low and high doped LPC-Si, respectively. Since we are focusing on intrinsic properties of LPC-Si on glass, the effective minority diffusion length (L_{eff}) was calculated by neglecting back surface recombination. By using SRV_{front} of 200 cm/s, τ of 1.8 µs and 0.8 µs give L_{eff} of 30 µm and 20 µm, respectively. These L_{eff} values are in good agreement with results obtained from previous device modeling of the other 13.2% efficiency cells using the ASPIN3 simulation package and light beam induced current (LBIC) measurement with line scan analysis [22, 34]. In this study, N_D of 8×10^{16} cm^{-3} was chosen for IBC cell simulation and experiment since it offers a reasonable compromise between J_{sc} and V_{oc} [13]. τ of 1.0 µs was obtained for this doping concentration. With τ of 1.0 µs and SRV_{front} of 200 cm/s, a L_{eff} of 24 µm is obtained. Simulated J_{sc} obtained from this simulation are displayed in Fig. 3(a).

In order to investigate the dependence of resistive loss on W_{BSF} variation, R_s was estimated. Contact resistances were chosen to be (60 ± 10) mΩcm² and (335 ± 70) mΩcm² for Si/aSi:H(n)/ITO/Ag and Si/aSi:H(i/p)/ITO/Ag contacts, respectively [22]. The calculation method of R_s based on geometry of IBC-SHJ cell is reported in [35]. The fill factor (*FF*) is calculated with the equation [36]:

$$FF = FF_0(1 - \frac{R_s \times J_{sc}}{V_{oc}}) . \quad (3)$$

FF_0 is determined for W_{BSF}=120 µm with *FF* of 74.7% as obtained in Ref. [22].

Simulated J_{sc} and calculated *FF* as a function of W_{BSF} are shown in Fig. 3(a). One can see that J_{sc} decreases sharply with increase in W_{BSF} due to the decrease in amount of photo-generated carriers in the emitter region. However, an increase in W_{BSF} leads to a decrease in contact resistance at BSF region, thus *FF* increases. *FF* increases gradually with an increase in W_{BSF} as soon as W_{BSF} exceeds 60 µm. Assuming that V_{oc} is 640 mV and 650 mV, the cell efficiency (η) can reach highest value at a W_{BSF} of 60 µm (Fig. 3(b)). For W_{BSF} > 60 µm, η is dominated by the decrease in J_{sc}. Therefore, a sharp decrease in η can be seen as W_{BSF} increases.

3.2. Experimental results

We fabricated more than 150 cells with various W_{BSF} on sixteen 5×5 cm^2 samples. Only cells without shunting issues (pseudo fill factor (*pFF*) ≥ 70% from *Suns-Voc* measurement) were taken into account. Fig. 4 shows J_{sc}, V_{oc}, *FF* and η of these cells as a function of W_{BSF}. A clear trend of decrease in J_{sc} when W_{BSF} increases can be seen. V_{oc} and η are comparable for all samples. The mean *FF* increases with increasing W_{BSF} as in the simulation results. This is also in agreement with the R_s extracted from the comparison of dark and illumination *J-V* curves shown in Fig. 5. *FF*s of more than 70% were achieved for W_{BSF} of 240 µm, 120 µm and 60 µm. One can see in Fig. 5 that there is a large deviation for the average R_s from theoretical values. It might be related to the variation of doping concentration or contact resistance due to inhomogeneity in surface texture and/or absorber quality. However, for some of the best cells with low R_s, an agreement in theoretically and experimentally determined R_s can be observed.

Fig. 6 displays the *J-V* curves of the best cell performance for each W_{BSF}. The parameters are listed in Table 2. The cells were measured with an additional anti-reflective foil (ARF) on the glass side to enhance light trapping [37]. By using an ARF, J_{sc} can gain up to 10%, raising efficiency around 10%. The highest efficiency is 14.2% for the cell with W_{BSF} of 120 µm, becoming a new record for (IBC-SHJ cell) for LPC-Si on glass. This efficiency is higher than that of IBC-SHJ cell of nano-textured 10 µm-mono c-Si absorber (13.7%) [38]. It is also equivalent to the efficiency of state of the art a-Si:H/µc-Si:H/µc-Si:H triple junction cell (14%) [39]. The highest obtained V_{oc} value was 661 mV. This value is comparable with a V_{oc} of state of the art multi-crystalline Si cell [9, 40]. The results indicate the high potential of LPC-Si on glass in thin-film solar cell application.

3.3. Discussion

3.3.1. Cell performance with various BSF widths

In this part, we took parameters of the best performance cell without ARF for each W_{BSF} to make a comparison, as displayed in Table 2. An efficiency of 13.6% is obtained for a W_{BSF} of 60 µm. For cells with W_{BSF} of 240 µm, the highest V_{oc} value of 661 mV was achieved. This high V_{oc} implies that this cell might lie on a very good grains with a low grain boundary density. However, the *FF* of 70.2% limits the efficiency to 12.8%. Theoretically, the highest *FF* would be obtained for the largest W_{BSF} since it has the lowest contact resistance. A possible reason for lower experimental *FF* is that this cell is located on grains with strongly tilted pyramids or flat surfaces, so that surface area is smaller, thus, the contact resistance is higher. Such a scenario could also explain why this cell has a high V_{oc} since back-surface passivation is better on flat surfaces than textured surfaces. In order to estimate the potential of the cells with W_{BSF} of 60 µm and 240 µm, we recalculated the *FF* of these cells based on the *FF* of the cell with W_{BSF} of 120 µm because for this W_{BSF} the experimental *FF* fits very good with the theoretical one determined by simulation. For these cells, a *FF* of 75.9% and 72.8% can be achieved, as shown in Table 2. However, J_{sc} of the cell with W_{BSF} of 60 µm is lower than the simulated one, therefore its η is lower than that of the cell with W_{BSF} of 120 µm. A simulated J_{sc} of 27.8 mA/cm^2 can be found with W_{BSF} of 60 µm, leading to η of 13.1% and η of 14.4% can be estimated for the cell measured with ARF. The reason for lower experimental J_{sc} might be due to the difference in absorber quality of these cells, such as more grain boundaries or dislocations. N_D of these samples is in the range of 8×10^{16} cm^{-3}, which lies between low and high doping cell reported in Ref. [22]. However, the V_{oc} is higher than the V_{oc} in the 13.2% efficiency cell with high doped absorber. This fact implies that samples in this study might have better absorber quality and/or surface passivation quality than the previous ones. In the next section, we will clarify the key factors contributing to the improvement of the cell performance by comparing the 14.2% efficiency cell in this study to the 13.2% efficiency cells reported in [22].

3.3.2. The route to the efficiency of 14.2% in comparison to 13.2% cell

In this part, we will analyze the surface recombination, the bulk quality as well as the series resistance of the 14.2% efficiency cell in comparison to the previous 13.2% efficiency cells in order to clarify which factors contributed significantly to the improvement in efficiency. All experimental parameters of these cells are listed in Table 3.

3.3.2.1. Front surface recombination and bulk quality analysis.

Fig. 7 shows the absorption spectra of all layers in the 14.2% efficiency cell. The blue dotted curve displayed absorption calculated from measured reflection (*R*) and transmission (*T*) spectra (*1-R-T*). Notice that the 14.2% efficiency cell was obtained for a sample with ON(ON) IL while the 13.2% efficiency cells were obtained for a sample with ONO IL. Therefore, the reflectance is different between these cells. The higher absorption in long wavelength region can make the 13.2% efficiency cells gain a calculated J_{sc} of 0.6 mA/cm^2 higher than J_{sc} of the 14.2% efficiency cell, as shown in Figs. 2 and 7. Therefore, 13.2% efficiency cells has more potential in J_{sc} than the 14.2% efficiency cell. As shown in Fig. 7, a potential J_{sc} of 32.7 mA/cm^2 can be achieved for the 14.2% efficiency cell. Assuming a V_{oc} of 661 mV and *FF* of 74.9% as demonstrated in this study, a high efficiency of 16% seems feasible.

We used extracted absorption spectra from GenPro4 to calculate the charge carrier generation profiles in LPC-Si. Experimental data of 14.2% efficiency cell was modeled using TCAD Sentaurus^{TM} to evaluate surface passivation and bulk quality. SRV_{front} and τ were varied to obtain experimental V_{oc} of 650 mV and J_{sc} of 26.53 mA/cm^2. For simple approach, we firstly assumed that the bulk quality does not change when ONO or ON(ON) IL is used. τ of 1 µs, which corresponds to bulk quality of LPC-Si using ONO IL, as mentioned in section 2.1, was used in this simulation. SRV_{front} was varied from 0 to 200 cm/s. The simulation results are shown in Fig. 8(a). One can see that J_{sc} increases strongly and V_{oc} increases slowly with decreasing SRV_{front}. Interestingly, even if SRV_{front} reduces to 0 cm/s, V_{oc} and J_{sc} cannot reach the experimental values. That strongly indicates that the bulk quality of LPC-Si using ON(ON) IL must be improved.

Next, we assume that SRV_{front} does not change but the bulk quality does. A constant SRV_{front} of 200 cm/s, which corresponds to surface passivation quality of ONO IL was implemented into simulation. τ was varied from 1 µs to 1.55 µs. In this case, τ should be larger than 1 µs to get $J_{sc} \geq 26.0$ mA/cm^2. Simulated J_{sc} and V_{oc} are displayed in Fig. 8(b). One can see that when τ reaches 1.55 µs, J_{sc} is larger than 26.53 mA/cm^2, but V_{oc} is less than 650 mV. Therefore, SRV_{front} might be less than 200 cm/s. SRV_{front} of 100 cm/s was thus chosen for the simulation. Fig. 8(b) also shows J_{sc} and V_{oc} as function of τ at SRV_{front} of 100 cm/s. Simulated J_{sc} of 26.44 mA/cm^2 and V_{oc} of 640 mV match quite well to experimental data when τ equals 1.16 µs. However, the remaining difference of 10 mV of V_{oc} might be due to back-surface passivation since we used the same defect layer for 13.2% efficiency cells. Improvement in bulk quality of LPC-Si might have a positive effect on deposition of a-Si:H layers, thus, traps in defect layers should decrease. By reducing defect concentration in defect layer between LPC-Si and a-Si:H interface, V_{oc} of 650 mV and J_{sc} of 26.56 mA/cm^2 can be achieved for SRV_{front} of 100 cm/s and τ of 1.16 µs. These values fit well to the experimental values. Using this defect layer with SRV_{front} of 200 cm/s and τ of 1.35 µs, we also obtained V_{oc} of 651 mV and J_{sc} of 26.47 mA/cm^2, which also match quite well with the experimental V_{oc} and J_{sc}. However, bulk quality of absorber was improved with using ON(ON) IL, low SRV_{front} of 100 cm/s might be more reasonable since in LPC-Si technique, Si absorber is crystallized directly on the passivation layer.

In conclusion, a SRV_{front} of 100 cm/s and τ of 1.16 µs, which corresponding to a L_{eff} of 26 µm were estimated for LPC-Si absorber with ON(ON) IL. This IL benefits not only from field effect passivation of SiN_x layer but also from the homogeneous passivation quality layer created by N_2O plasma process. Therefore, SRV_{front} of sample using ON(ON) ILs is better than that of sample using ONO ILs. According to analysis, a homogeneous N-rich SiO_xN_y layer was formed on ON stack by plasma oxidation process and a smooth IL/ LPC-Si interface can be observed by TEM images [24]. This homogeneous layer might support a uniform shield for LPC-Si from dislocation and/ or stacking fault generation at the interface during the crystallization process, thus, suppressing surface recombination and enhancing bulk quality.

3.3.2.2.Series resistance analysis

One important factor contributing the 14.2% cell is the high *FF* of 74.9%, which was achieved thanks to low series resistance (R_s). Using comparison of dark and illuminated *J-V* curve method to calculate R_s, a value of 1.13 Ωcm^2 can be obtained for the cell. This value is close to the calculated R_s using contact resistances of 60 mΩcm² and 335 mΩcm² for

Si/aSi:H(n)/ITO/Ag and Si/aSi:H(i/p)/ITO/Ag contact, respectively. It is also lower than R_s of the 13.2% efficiency cell with high doped absorber even though its bulk resistance is slightly higher. Lower R_s might be due to lower contact resistance of 14.2% efficiency cell. Higher bulk quality might result from fewer grain boundaries and/or crystal defects on the Si surface, thus, resistance loss from contact on grain boundaries can be suppressed. Moreover, it also offers a less defect Si surface for initial texturing process, which might result in better pyramid formation, supporting a larger surface area, thus decreasing the contact resistance.

4. Outlook

From the presented device loss analysis it can be stated that the bulk quality of LPC-Si is a key factor to improve cell performance. A potential J_{sc} of 32.7 mA/cm^2 is feasible for 13 µm-thick cells without using any ARF, resulting in a cell with η of 16% by assuming the highest V_{oc} and *FF* in this study (661 mV; 74.9%) are achieved. An estimated J_{sc} of 27.8 mA/cm^2 was obtained for the current quality of LPC-Si, in which SRV_{front} of 100 cm/s and τ of 1.16 µs are representative values. They correspond to a L_{eff} of 26 µm, which is still lower than half of W_{BSF}. Cell efficiency is mainly limited by recombination at grain boundaries and dislocations. In order to get $L_{eff} \geq$30 µm, τ should be increased further to values exceeding 1.6 µs. Then an estimated J_{sc} of 29.0 mA/cm^2 can be achieved. A SRV_{front} <10 cm/s also can improve cell efficiency, however, it is a challenge to achieve this low *SRV* for LPC-Si surface passivation technique, since the passivation layer need to be stable during the crystallization process. Methods to enhance bulk quality, such as passivating LPC-Si by H-rich SiN_x firing or phosphorus gettering may be promising approaches. By increasing the LPC-Si thickness to 24 µm, which is close to L_{eff}, potential J_{sc} becomes 33.9 mA/cm^2. In order to further increase J_{sc}, it would be effective to reduce optical losses, e.g. decreasing ITO thickness, using nano imprinting at front Si surface [41-45], or optimization of back surface texturing. Optimization of N_d is also a crucial step to increase cell efficiency. According to simulation, a moderate doping with N_d of 4×10^{16} cm^{-3} is the optimum value for both 120 µm and 60 µm, as shown in Fig. 9. It is in good agreement with 1-D device simulations indicating that ideal dopant concentration of absorber thicknesses of 10-20 µm is 2-6×10^{16} cm^{-3} [13]. In order to increase *FF*, reducing contact resistance, especially at BSF contact should be considered. A nano-crystalline (nc)-Si:H film would be a nice option since it has higher conductivity than a-Si:H films. More importantly, improvement in back surface passivation of LPC-Si is still hidden factor and need further investigation for LPC-Si.

5. Summary

In conclusion, an efficiency as high as 14.2% was achieved for an IBC-SHJ cell of LPC-Si on glass, thanks to the improvement in surface passivation and bulk quality by using ON(ON) ILs and development in cell fabrication processes. A mean V_{oc} of 620 mV and highest V_{oc} of 661 mV show the potential of LPC-Si in thin film solar cell technology. The absorption profile of the back-textured LPC-Si layer stack was simulated with GenPro4. The modeling of the IBC-SHJ solar cell was carried out by TCAD-Sentaurus^{TM}. The 2D simulation results showed best agreement with experimental data for SRV_{front} = 100 cm/s and τ = 1.16 µs, which correspond to a L_{eff} of 26 µm. According to simulated data, N_d of 4×10^{16} cm^{-3} and W_{BSF} of 60 µm are optimum values to maximise the cell efficiency. A potential efficiency of 16% was also estimated for the cells. However, at the present state the cell efficiency is limited by the bulk quality, a carrier lifetime of 1.16 µs is not enough to achieve cells with efficiencies above 20%. In order to get an efficiency comparable to mc-Si cells (21.5%), besides techniques to enhance the absorber

quality, it is necessary to introduce effective light trapping or light coupling technique to increase J_{sc} to values exceeding 32 mA/cm^2.

Acknowledgment

The authors would like to thank DSM Advanced Surfaces for providing the textured light-trapping anti-reflection foil (ARF) and GP Solar for providing the Alkatex IPA-free texturing agent; R. Santbergen (TU-Delft) and D. Eisenhauer for optical simulation advices and support with GenPro4; J-C. Stang and G. Chistiakova for support with TCAD-Sentaurus^{TM} simulations; J-C. Stang, L. Korte and T. Frijnts for interesting discussion; PECVD (AKT) team (PVcomB) for great help of a-Si:H film deposition; K. Jacob, M. Wittig, M. Hartig and K. M-Stillrich in solar cell preparation.

References

[1] Int. Technol. Roadmap Photovoltaics. (2016). Int. Technol. Roadmap Photovoltaic. Results, 2016, Rev. 1 [Online]. Available: www.itrpv.net
[2] International Renewable Energy Agency, Renewable Energy Cost Analysis-Solar Photovoltaics (2012)
[3] K. R. Catchpole, M.J. McCann, K.J. Weber, A.W. Blakers, A review of thin-film crystalline silicon for solar cell applications. Part 2: Foreign substrates, Sol. Energy Mater. Sol. Cells 68-2 (2001) 173-215.
[4] T. Matsuyama, N. Terada, T. Baba, T. Sawada, S. Tsuge, K. Wakisaka, S. Tsuda, High-quality polycrystalline silicon thin film prepared by a solid phase crystallization method, J. of Non-Cryst. Solids 198-2 (1996) 940-944.
[5]I. Gordon, L. Carnel, D. Van Gestel, G. Beaucarne, J. Poortmans, 8 % efficient thin-film polycrystalline-silicon solar cells based on aluminum-induced crystallization and thermal CVD, Progress in Photovoltaics: Research and Applications 15 (2007)
[6] L. Carnel, I. Gordon, D. Van Gestel, G. Beaucame, J. Poortmans, Efficient soar cells based on fine-grained polysilicon, Thin Solid films 516 (2008) 6839-6843.
[7] C. Becker, D. Amkreutz, T.Sontheimer, V. Preidel, D. Lockau, J. Haschke, L. Jogshies, C. Klimm, J. J. Merkel, P. Plocica, S. Steffens, B. Rech, Polycrystalline silicon thin-film solar cells: Status and perspectives, Sol. Energy Mater. Sol. Cells 119 (2013) 112-123.
[8] J. Dore, D. Ong, S. Varlamov, R. Egan, M.A. Green, "Progress in laser-crystallized thin-film polycrystalline silicon solar cells: Intermediate layers, light trapping and metallization", IEEE Journal of Photovoltaics 4, 2014, pp. 33-39
[9] S. Kühnapfel, N.H. Nickel, S. Gall, M. Klaus, C. Genzel, B. Rech, D. Amkreutz, "Preferential {100} grain orientation in 10 micrometer-thick laser crystallized multicrystalline silicon on glass", Thin Solid Films 576 (2015) 68-74.
[10] J. Haschke, D. Amkreutz, L. Korte, F. Ruske, B. Rech, Towards wafer quality crystalline silicon thin-film solar cells on glass, Sol. Energy Mater. Sol. Cells 128 (2014) 190-197.
[11] J. Haschke, D. Amkreutz, B. Rech, "Liquid phase crystallized silicon on glass: Technology, material quality and back contacted heterojunction cells", Jpn. J. Appl. Phys. 55 (2016) 04EA04 1-10.
[12] O. Schultz, S. W. Glunz, G. P. Willeke, Multicrystalline silicon solar cells exceeding 20% efficiency, Prog. Photovolt. Res. Appl. 12(7) (2004) 553–558.
[13] D. Amkreutz, J. Haschke, S. Kühnapfel, P .Sonntag, B. Rech, Silicon thin-film solar cells on glass with open-circuit volatges above 620 mV formed by Liquid-phase crystallization, IEEE J. Photovoltaics. 4-6 (2014) 1496-1501.
[14] O. Gabriel, T. Frijnts, N. Preissler, D. Amkreutz, S. Calnan, S. Ring, B. Stannowski, B. Rech, R. Schlatmann, Crystalline silicon on glass-interface passivation and absorber material quality, Prog. Photovoltaics Res. Appl. 24-2 (2016) 1499 -1512.
[15] N. Preissler, D. Amkreutz, P. Sonntag, M. Trahms, R. Schlatmann, B. Rech, Interface engineering for liquid-phase crystallized-silicon solar cells on glass, Sol. RRL 1 3-4 (2017) 1700015 1-5.
[16] J. Dore, S. Varlamov, M.A. Green, Intermediate layer development for laser –crystallized thin-film silicon solar cells on glass, IEEE J. Photovoltaics 5 (2015) 9-16.
[17] J. Haschke, D. Amkreutz, T. Frijnts, S. Kuhnapfel, T. Hanel, B. Rech, Influence of barrier and doping type on the open-circuit voltage of liquid phase-crysllized silicon thin-film solar cells on glass, IEEE J. Photovoltaics 5-4, 1001 (2015) 1001-1005.
[18] D. Amkreutz, W.D. Barker, S. Kuhnapfel, P. Sonntag, O. Gabriel, S. Gall, U. Bloeck, J. Schmidt, J. Haschke, B. Rech, Liquid-phase crystallized silicon solar cells on glass: Increasing

the open-circuit voltage by optimized interlayers for n- and p-type absorbers, IEEE J. Photovoltaics 5, 1757 (2015).
[19] J. Schmidt, B. Veith, R. Brendel, Effective surface passivation of crystalline silicon using ultrathin Al_2O_3 films and Al_2O_3/SiN_x stacks, Phys. Status Solidi: Rapid Res. Lett. 3-9 (2009) 287-289.
[20] T. Frijnts, S. Kühnapfel, S. Ring, O. Gabriel, S. Calnan, J. Haschke, B. Stannowski, B. Rech, R. Schlatmann, Analysis of photo-current potentials and losses in thin film crystalline silicon solar cells, Sol. Energy Mater. Sol. Cells 143 (2015) 457-466.
[21] P. Sonntag, J. Haschke, S. Kühnapfel, O. Gabriel, D. Amkreutz, B. Rech, Properties of liquid phase crystallized interdigitated back-contact solar cells on glass. Energy Procedia 77 (2015) 487–492.
[22] P. Sonntag, N. Preissler, M. Bokalič, M. Filipič, M. Trahms, J. Haschke, R. Schlatmann Marko Topič, B. Rech, D. Amkreutz, Silicon solar cells on glass with power conversion efficiency above 13 % at thickness below 15 micrometer, Sci. Rep. 7 (2017) 873 1-12.
[23] P. Sonntag, M. Bokalič, M. Filipič, T. Frijnts, D. Amkreutz, Marko Topič, B. Rech, Analysis of local minority carrier diffusion lengths in liquid phase crystallized silicon thin-film solar cells", IEEE Journal of Photovoltaics 7-1 (2017) 32-36.
[24] N. Preissler, C. T. Trinh, M. Trahms, P. Sonntag, D. Abou-Ras, H. Kirmse, R. Schlatmann, B. Rech, D. Amkreutz, Impact of dielectric layers on front-side passivation of liquid phase crystallized silicon solar cells on glass, in Proceedings of the 44th IEEE PVSC, 2017 (submitted).
[25]D. Pysch, A. Mette, S.W. Glunz, A review and comparison of different methods to determine the series resistance of solar cells, Sol. Energy Mater. Sol. Cells 91 (2007) 1698-1706.
[26] SYNOPSYS. Sentaurus Structure Editor User Guide. F-2011.09, September 2011
[27] R. Santbergen, T. Meguro, T. Suezaki, G. Koizumi, K. Yamamoto, and M. Zeman, GenPro4 optical model for solar cell simulation and its application to multifunction solar cells, IEEE journal of photovoltaics 7-3 (2017) 919-926.
[28] C.V. Cushman, B.A. Sturgell, A.C. Martin, B.M. Lunt, N.J. Smith, and M.R. Linford, Eagle XG® glass, optical constants from 230 to 1690 nm (0.73-5.39 eV) by spectroscopic ellipsometry, Surf. Sci. Spectra 23 (2016) 55-60.
[29] M.A. Green, Self-consistent optical parameters of intrinsic silicon at 300 K including temperature coefficients, Sol. Energy Mater. Sol. Cells 92 (2008) 1305-1310.
[30] D. Zhang, I.A. Digday, R. Santbergen, R.A.C.M.M. van Swaaij, P. Bronsveld, M. Zeman, J.A.M. van Roosmalen, A.W. Weeber, Design and fabrication of SiOx/ITO double-layer anti-reflective coating for heterojuction silicon solar cells, Sol. Energy Mater. Sol. Cells 117 (2013) 132.
[31] P. B. Johnson and R. W. Christy, Optical Constants of Noble Metals, Physical Review B, Volume 6, Number 12, 1972, pp. 4370-4379
[32] J. G. Fossum and D. S. Lee, A physical model for the dependence of carrier lifetime on doping density in nondegenerate silicon, Solid-State Electron. 25-8 (1982) 741-747.
[33] J. G. Fossum, Computer-aided numerical analysis of silicon solar cells, Solid-State Electronics 19 (1976) 269-277.
[34] M. Filipič, Z.C. Holman, F. Smole, S. De Wolf, C. Ballif, M. Topič, Analysis of lateral transport through the inversion layer in amorphous silicon/crystalline silicon heterojunction solar cells, J. Appl. Phys. 114 (2013) 74504.
[35] Y. Yang, G. Xu, K. Zhang, X. Zhang, H. Shen, P. A. Altermatt, P. J. Verlinden, Z. Feng, Analysis of series resistance of industrial crystalline silicon solar cells by numerical simulation and analytical modelling, in Proc. 28th Eur. Photovoltaic Sol. Energy Conf. Exhib. (2013) 1559-1561.

[36] M. A. Green. Solar cells: Operating principles, technology, and system applications, Prentice-Hall Inc., Englewood Cliffs, 1982, p. 288
[37] C. Ulbrich, A. Gerber, K. Hermans, A. Lambertz, U. Rau, Analysis of short circuit current gains by an anti-reflective textured cover on silicon thin film solar cells. Prog. Photovoltaics Res. Appl. 21 (8), (2013) 1672.
[38] S. Jeong, M.D. McGehee, Y. Cui, All-back-contact ultra-thin silicon nanocone solar cells with 13.7% power conversion efficiency, Nat. Commun. 4 (2013) 2950 1-7.
[39] H, Sai, T. Matsui, K. Matsubara, Stabilized 14.0% -efficient triple-junction thin-film silicon solar cell", Appl. Phys. Lett. 109 (2016) 183506 1-5.
[40] Martin A. Green, Corrigendum to Solar cell efficiency tables (version 49), Prog. Photovolt: Res. Appl. 24 (2016) 905-913.
[41] G. Köppel, V. Preidel, S. Mangold, E. Rudigier-Voigt, M. Hývl, A. Fejfar, B. Rech, C. Becker, Nanoimprint-textured glass superstrates for light trapping in crystalline silicon thin-film solar cells, Energy Procedia 84 (2015) 118-126.
[42] C. Becker, V. Preidel, D. Amkreutz, J. Haschke, B. Rech, Double-side textured liquid phase crystallized silicon thin-film solar cells on imprinted glass, Sol. Energy Mater. Sol. Cells 135 (2015) 2-7
[43] G. Köppel, B. Rech, C. Becker, Sinusoidal nanotextures for light management in silicon thin-film solar cells, Nanoscale 8 (2016) 8722-8728.
[44] D. Eisenhauer, G. Köppel, K. Jäger, D. Chen, O. Shargaieva, P. Sonntag, D. Amkreutz, B. Rech, C. Becker, Smooth anti-reflective three-dimensional textures for liquid phase crystallized silicon thin-film solar cells on glass. Sci. Rep. 7 (2017) 2658 1-10.
[45] K. Jäger, C. Barth, M. Hammerschmidt, S. Herrmann, S. Burger, F. Schmidt, C. Becker, Simulations of sinusoidal nanotextures for coupling light into c-Si thin-film solar cells, Opt. Express 24 (2016) A569-A580

Figure captions

Fig. 1. Top-view from back side of a sample after (a) emitter structuring (b) back surface field structuring (c) electrodes structuring. (d) Cross sectional structure of an IBC-SHJ cell.

Fig. 2. (a) AFM image of a textured LPC-Si on glass. (b) Absorption spectra of all layers in an IBC-SHJ cell with ONO IL simulated by GenPro4. Blue dot curve indicates experimental 1-R-T of this sample.

Fig. 3. (a) J_{sc} and *FF* as functions of W_{BSF}. J_{sc} are simulated values from 2D-simulation with τ of 1 μs, SRV_{front} of 200 cm/s and N_D of 8×10^{16} cm^{-3} are input parameters for LPC-Si. *FFs* are obtained from Equation (3). (b) Efficiency (η) of IBC cell with various W_{BSF} at V_{oc} of 640 and 650 mV.

Fig. 4. Experimental J_{sc}, V_{oc}, *FF* and η as a function of W_{BSF}.

Fig. 5. R_s determined from comparison of dark and illuminated *J-V* curves at various W_{BSF}. Star dots represent theoretical value calculated based on geometry of IBC-SHJ cell following Ref [35].

Fig. 6. The *J-V* curves of the best cells with W_{BSF} of 60, 120 and 240 μm.

Fig. 7. Absorption spectra of all layers in an IBC-SHJ cell with ON(ON) IL simulated by GenPro4. Blue dot curve indicates experimental *1-R-T* of this sample. Experimental *1-R-T* of the sample with ONO IL is also shown in asterisk curve for comparison.

Fig. 8. (a) J_{sc} and V_{oc} as functions of SRV_{front} at τ of 1 μs. (b) Dependence of J_{sc} and V_{oc} on τ at SRV_{front} of 100 and 200 cm/s. Blue and black lines represents for the experimental V_{oc} and J_{sc}, respectively. Opened and filled stars display simulated J_{sc} and V_{oc} with lower defect concentration at a-Si:H/LPC-Si interface.

Fig. 9. Simulated efficiency as a function of N_D with W_{BSF} of 60 μm.

Table 1. Experimental and simulated data of cells with different $N_{D.}$ Experimental data of low and high doped cells are taken from Ref. [22]. J_{sc} and V_{oc} for medium doped cell are simulated results with input parameters extracted from simulation for low and high doped cells.

Cell Doping level	N_D (cm^{-3})	V_{oc} (mV)		J_{sc} (mA/cm^2)		*SRV* (cm/s)	τ (μs)	L_{eff} (μm)
		Experimental	Simulated	Experimental	Simulated			
Low	1.2×10^{16}	620	613	28.1	28.1	200	1.8	30
High	1.2×10^{17}	635	636	25.2	25.2	200	0.8	20
Medium*	8×10^{16}	--	635	--	27.4	200	1.0	24

Table 2. Cell parameters at different W_{BSF} with and without ARF. *FF* and η after *FF* recalculation also listed for comparison.

W_{BSF}		J_{sc} (mA/cm^2)	V_{oc} (mV)	*FF* (%)		*Ƞ* (%)	
				Experimental	Recalculate	Experimental	Recalculate
240 μm	With ARF	26.9	661	72.20	75.98	12.84	13.51
	Without ARF	25.197	651	72.50	75.98	11.89	12.46
120 μm	With ARF	28.978	654	74.94	74.94	14.20	14.20
	Without ARF	26.53	650	74.84	74.84	12.91	12.91
60 μm	With ARF	29.683	646	70.94	72.73	13.61	13.95
	Without ARF	27.143	639	70.94	72.73	12.34	12.61

Table 3. Cell parameter of the best cell in this study and 13.2% efficiency cells from Sonntag et al. [22]. The cells were measured with and without ARF.

Cell	ILs	N_D (cm^{-3})	W_{BSF}		J_{sc} (mA/cm^2)	V_{oc} (mV)	FF (%)	η (%)
Sonntag *et. al*	ONO	1.2×10^{16}	120 µm	With ARF	31.3	626	67.2	13.2
				Without ARF	28.1	620	67.2	11.9
Sonntag *et. al*	ONO	12×10^{16}	120 µm	With ARF	27.5	642	74.7	13.2
				Without ARF	25.2	635	74.7	11.9
This study	ON(ON)	8×10^{16}	120 µm	With ARF	28.98	654	75	14.21
				Without ARF	26.53	650	75	12.91

Fig. 1

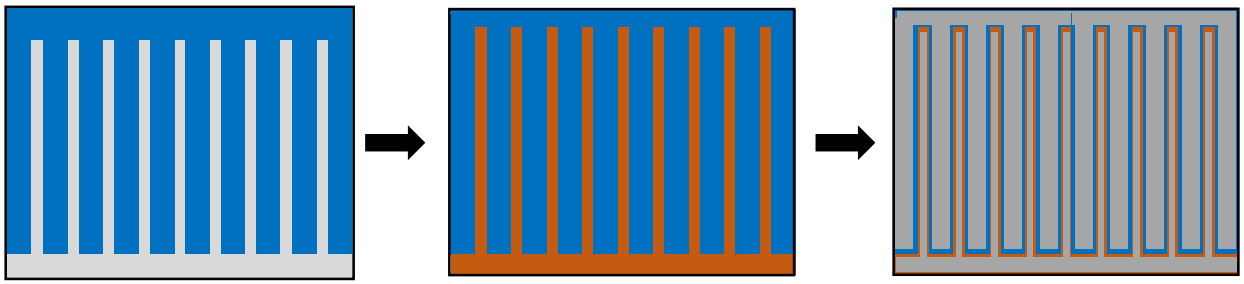

After emitter structuring (a)

After BSF structuring (b)

After electrodes structuring (c)

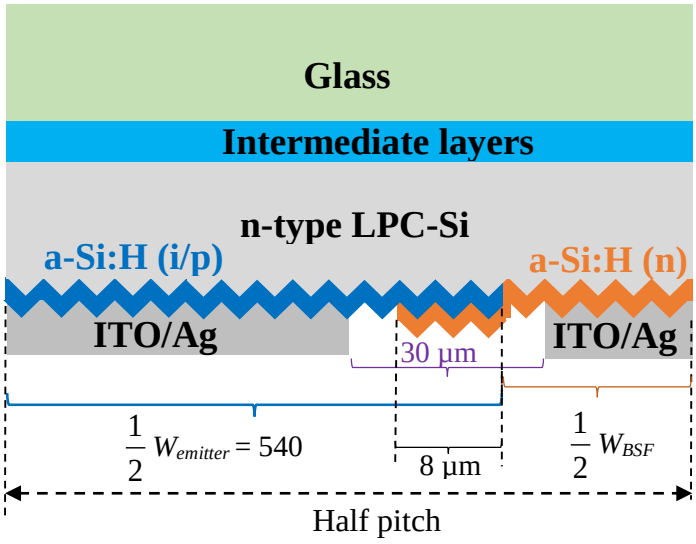

(d)

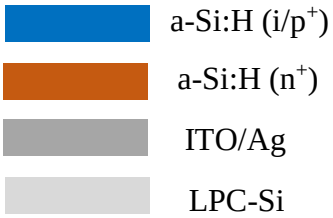

Fig. 2

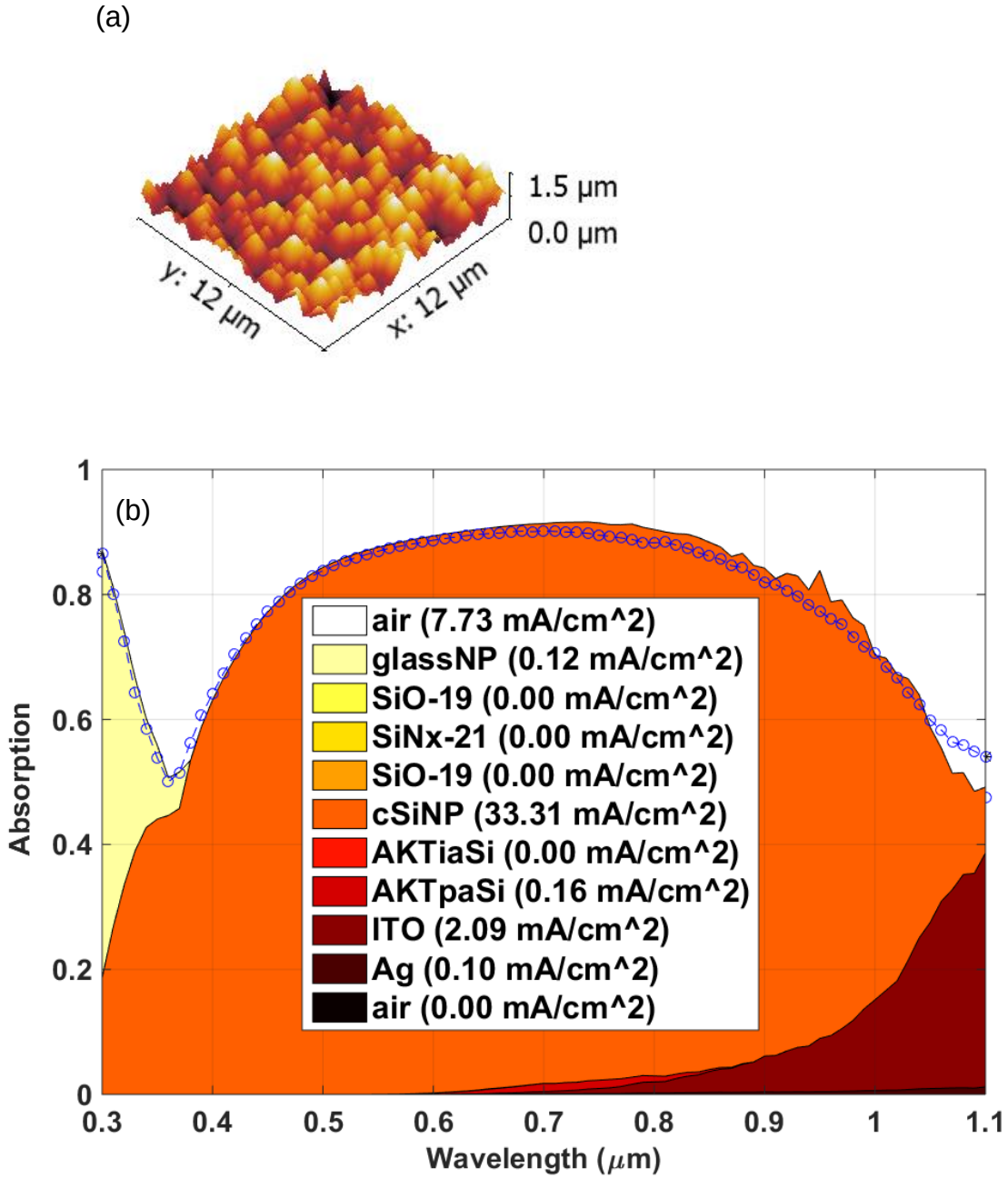
(a)
1.5 µm
0.0 µm
y: 12 µm
x: 12 µm
(b)
air (7.73 mA/cm^2)
glassNP (0.12 mA/cm^2)
SiO-19 (0.00 mA/cm^2)
SiNx-21 (0.00 mA/cm^2)
SiO-19 (0.00 mA/cm^2)
cSiNP (33.31 mA/cm^2)
AKTiaSi (0.00 mA/cm^2)
AKTpaSi (0.16 mA/cm^2)
ITO (2.09 mA/cm^2)
Ag (0.10 mA/cm^2)
air (0.00 mA/cm^2)
Absorption
Wavelength (µm)
0
0.2
0.4
0.6
0.8
1
0.3
0.4
0.5
0.6
0.7
0.8
0.9
1
1.1

Fig. 3

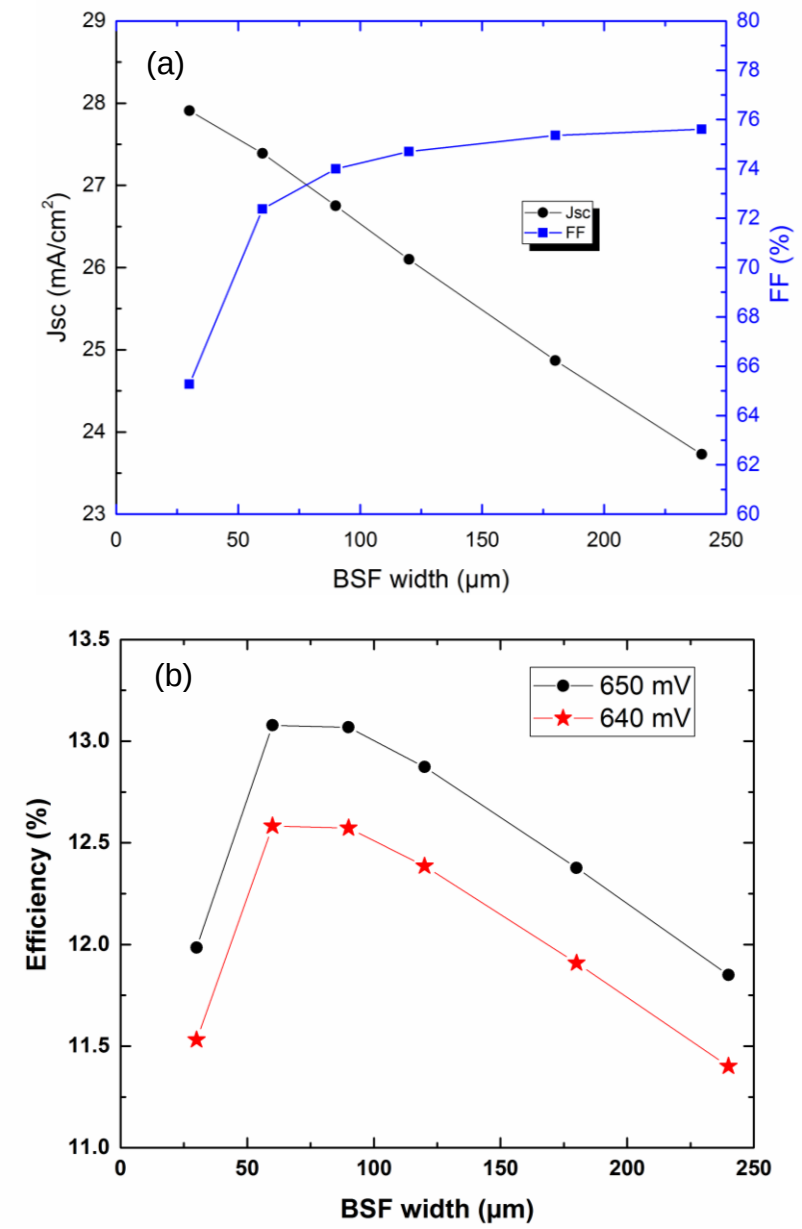
(a)
Jsc (mA/cm^2)
FF (%)
BSF width (μm)
Jsc
FF
(b)
Efficiency (%)
BSF width (μm)
650 mV
640 mV

Fig. 4

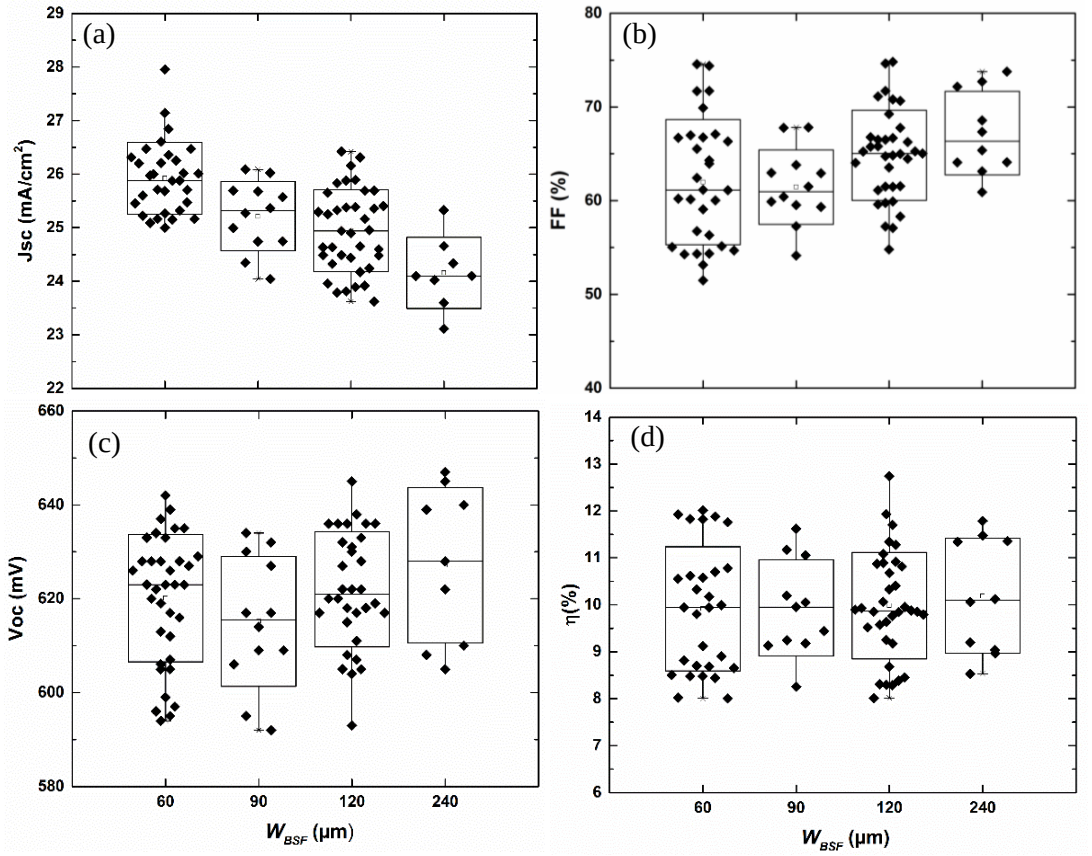
(a)
Jsc (mA/cm^2)
29
28
27
26
25
24
23
22
(b)
FF (%)
80
70
60
50
40
(c)
Voc (mV)
660
640
620
600
580
60
90
120
240
W_{BSF} (μm)
(d)
η(%)
14
13
12
11
10
9
8
7
6
60
90
120
240
W_{BSF} (μm)

Fig. 5

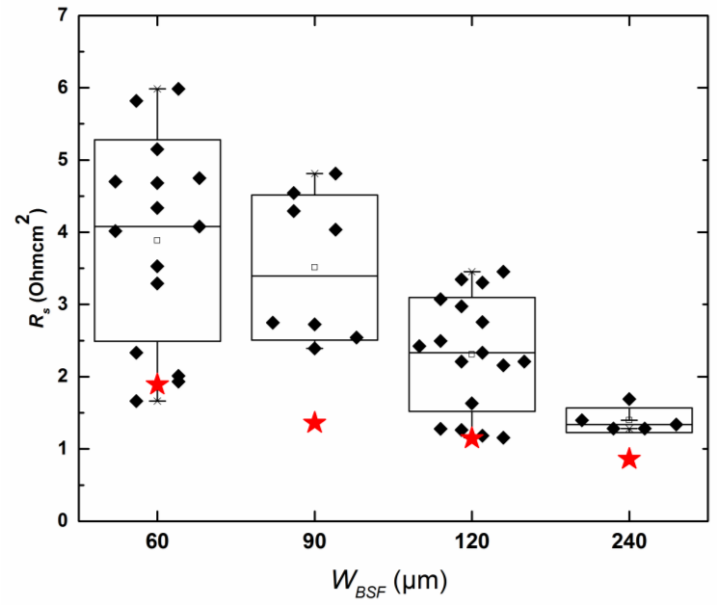

Fig. 6

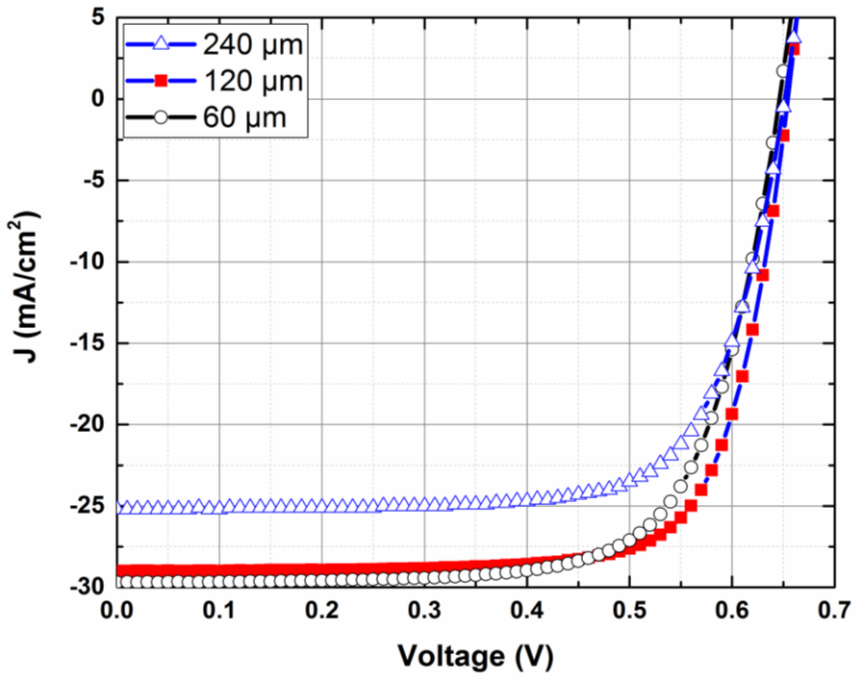
240 μm
120 μm
60 μm
J (mA/cm²)
Voltage (V)
5
0
-5
-10
-15
-20
-25
-30
0.0
0.1
0.2
0.3
0.4
0.5
0.6
0.7

Fig. 7

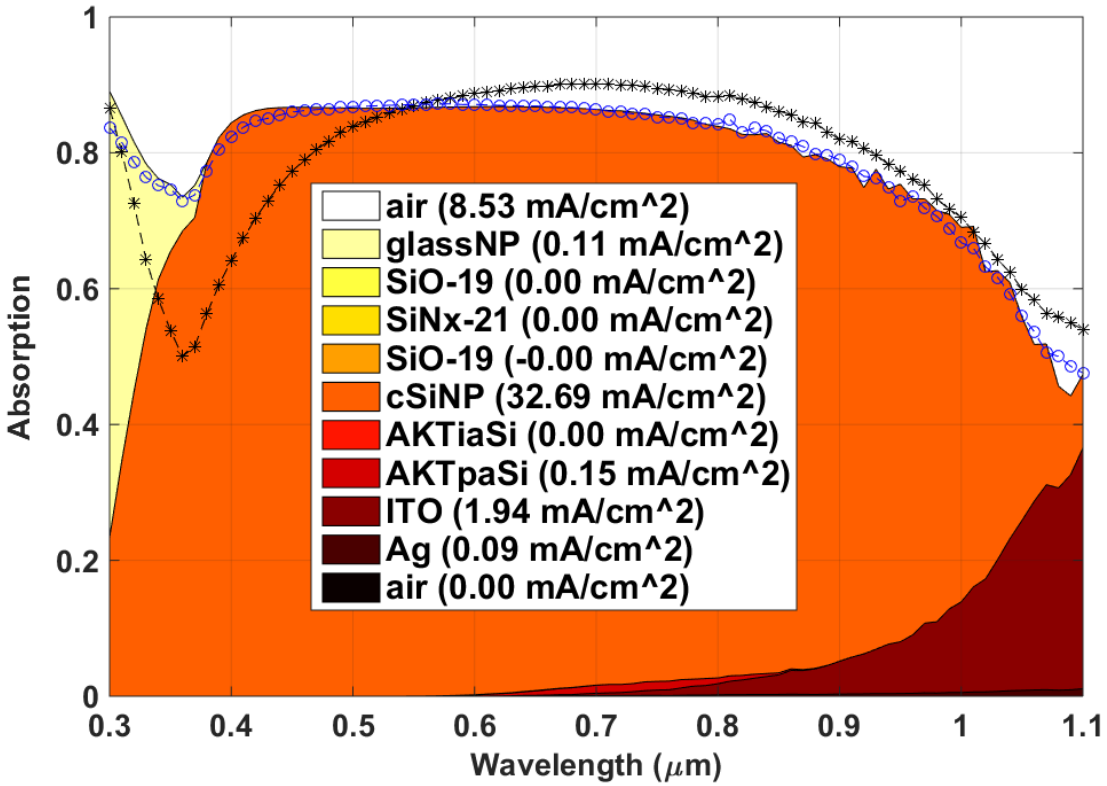
Absorption
Wavelength (μm)
air (8.53 mA/cm^2)
glassNP (0.11 mA/cm^2)
SiO-19 (0.00 mA/cm^2)
SiNx-21 (0.00 mA/cm^2)
SiO-19 (-0.00 mA/cm^2)
cSiNP (32.69 mA/cm^2)
AKTiaSi (0.00 mA/cm^2)
AKTpaSi (0.15 mA/cm^2)
ITO (1.94 mA/cm^2)
Ag (0.09 mA/cm^2)
air (0.00 mA/cm^2)

Fig. 8

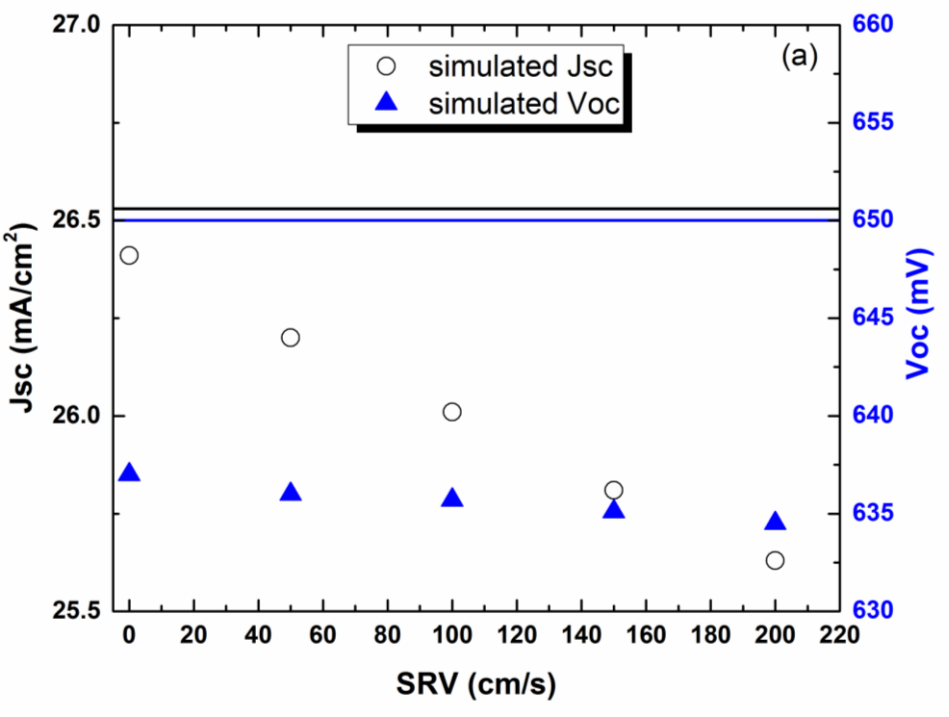
(a)
simulated Jsc
simulated Voc
Jsc (mA/cm^2)
Voc (mV)
SRV (cm/s)
27.0
26.5
26.0
25.5
660
655
650
645
640
635
630
0
20
40
60
80
100
120
140
160
180
200
220

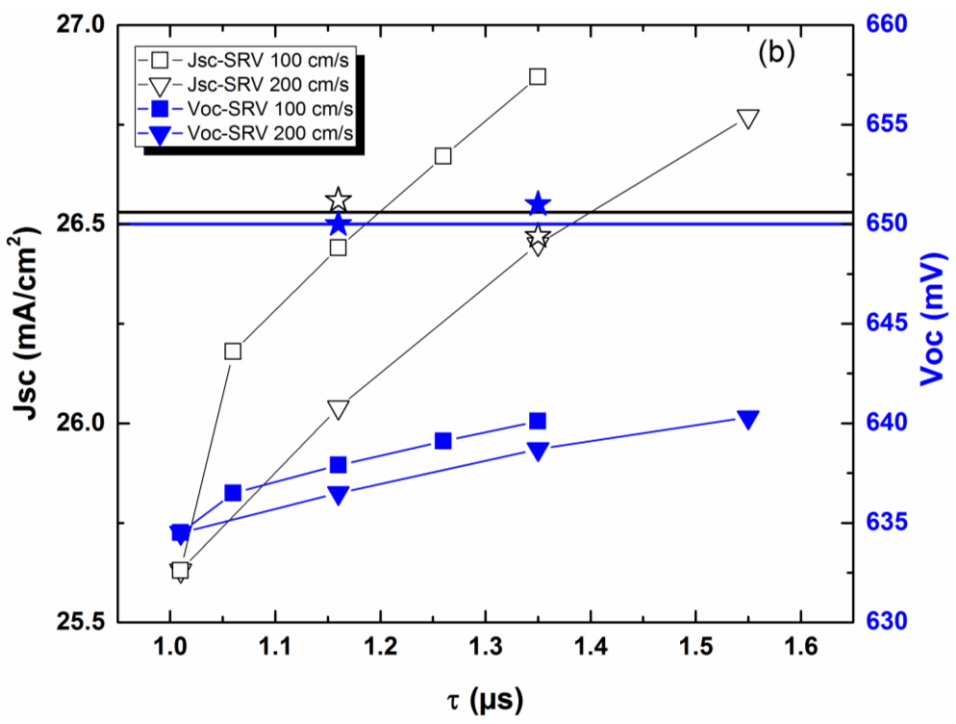
(b)
Jsc-SRV 100 cm/s
Jsc-SRV 200 cm/s
Voc-SRV 100 cm/s
Voc-SRV 200 cm/s
Jsc (mA/cm^2)
Voc (mV)
τ (μs)
27.0
26.5
26.0
25.5
660
655
650
645
640
635
630
1.0
1.1
1.2
1.3
1.4
1.5
1.6

Fig. 9

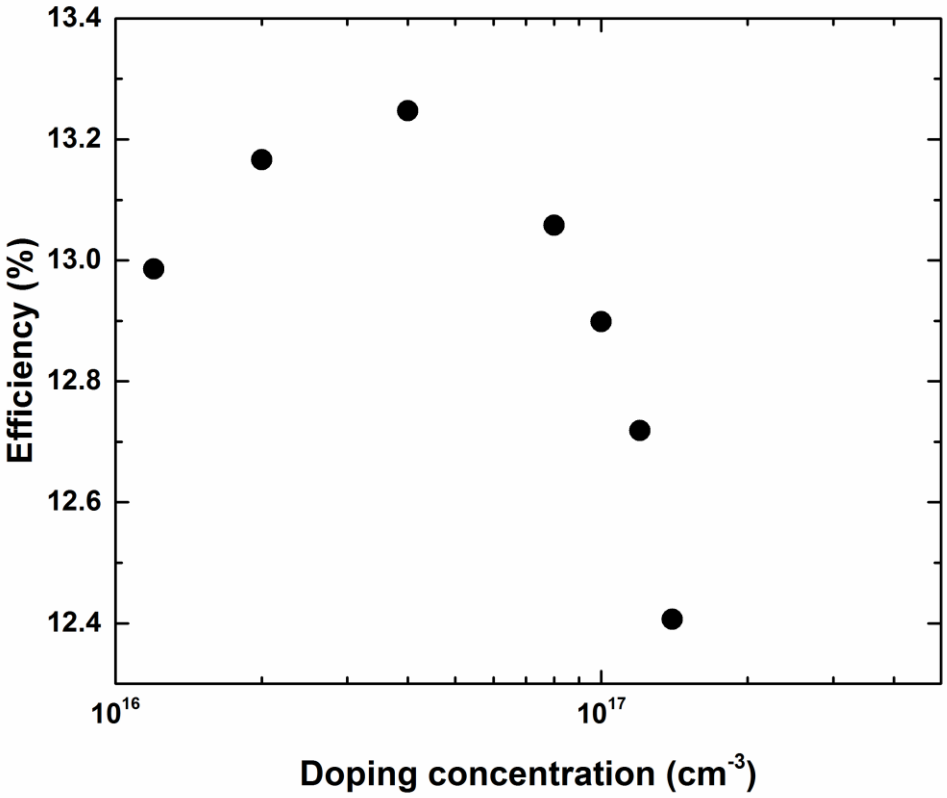
13.4
13.2
13.0
12.8
12.6
12.4
Efficiency (%)
10^16
10^17
Doping concentration (cm^-3)